Supplemental Material for "Robustness of Off-Axis Electron Vortices in Nonuniform Magnetic Fields"

Hui-Dong Huang,* Qi Meng,* Zhi-Bin Wang, Liang Lu, Jian Chen,† and Li-Ping Zou‡
Sino-French Institute of Nuclear Engineering and Technology, Sun Yat-Sen University, Zhuhai 519082, China

CONTENTS

S1 Landau-level algebra . . . 2

S2 Effective Hamiltonian and SU(1,1) structure . . . 4
A Decomposition of the effective Hamiltonian . . . 4
B SU(1,1) structure . . . 4
C Factorization of the unitary transformation . . . 4
D Transformation of the SU(1,1) generators . . . 5
E Interaction picture . . . 5
F Heisenberg equations in the interaction frame . . . 5
G Rotating frame and conserved norm . . . 6
H Return to the Schrödinger picture . . . 6

S3 Time evolution of the extrinsic OAM. . . . 7
A Heisenberg equations . . . 7
B Evolution of the extrinsic OAM. . . . 7

S4 First-principles numerical simulations . . . 9
A Propagation algorithm and initial-state wavefunction . . . 9
B Supplemental simulation results . . . 10

S5 Description of Supplemental Videos . . . 12

* These authors contributed equally to this work.
† Contact author: chenjian5@mail.sysu.edu.cn
‡ Contact author: zoulp5@mail.sysu.edu.cn

S1. LANDAU-LEVEL ALGEBRA

Starting from the canonical commutation relations

$$[\hat{r}_i, \hat{p}_j] = i\hbar\delta_{ij}, \qquad [\hat{r}_i, \hat{r}_j] = [\hat{p}_i, \hat{p}_j] = 0, \tag{S1}$$

and kinetic momentum commutator

$$[\hat{\pi}_x, \hat{\pi}_y] = -\mathrm{i}\hbar eB_0, \tag{S2}$$

we can construct the cyclotron and guiding-center coordinates as

$$\hat{\boldsymbol{\eta}} = -\frac{1}{eB_0}\mathbf{e}_z \times \hat{\boldsymbol{\pi}}, \qquad \hat{\mathbf{R}} = \hat{\mathbf{r}}_\perp - \hat{\boldsymbol{\eta}}, \tag{S3}$$

which, in components,

$$\hat{\eta}_x = \frac{1}{eB_0}\hat{\pi}_y, \quad \hat{\eta}_y = -\frac{1}{eB_0}\hat{\pi}_x, \quad \hat{X} = \hat{x} - \hat{\eta}_x, \quad \hat{Y} = \hat{y} - \hat{\eta}_y, \tag{S4}$$

satisfy

$$[\hat{\eta}_x, \hat{\eta}_y] = -\frac{i\hbar}{eB_0}, \qquad [\hat{X}, \hat{Y}] = \frac{i\hbar}{eB_0}, \qquad [\hat{\boldsymbol{\eta}}, \hat{\mathbf{R}}] = 0. \tag{S5}$$

We now introduce two pairs of ladder operator

$$\hat{a} = \sqrt{\frac{eB_0}{2\hbar}}(\hat{\eta}_x - i\hat{\eta}_y), \quad \hat{a}^\dagger = \sqrt{\frac{eB_0}{2\hbar}}(\hat{\eta}_x + i\hat{\eta}_y), \quad \hat{b} = \sqrt{\frac{eB_0}{2\hbar}}(\hat{X} + i\hat{Y}), \quad \hat{b}^\dagger = \sqrt{\frac{eB_0}{2\hbar}}(\hat{X} - i\hat{Y}). \tag{S6}$$

They satisfy:

$$[\hat{a}, \hat{a}^\dagger] = 1, \qquad [\hat{b}, \hat{b}^\dagger] = 1, \qquad [\hat{a}, \hat{b}] = [\hat{a}, \hat{b}^\dagger] = 0. \tag{S7}$$

Inverting these relations gives

$$\hat{\eta}_x = \sqrt{\frac{\hbar}{2eB_0}}(\hat{a} + \hat{a}^\dagger), \quad \hat{\eta}_y = i\sqrt{\frac{\hbar}{2eB_0}}(\hat{a} - \hat{a}^\dagger), \quad \hat{X} = \sqrt{\frac{\hbar}{2eB_0}}(\hat{b} + \hat{b}^\dagger), \quad \hat{Y} = -i\sqrt{\frac{\hbar}{2eB_0}}(\hat{b} - \hat{b}^\dagger). \tag{S8}$$

Hence the position operator decomposes as

$$\hat{\mathbf{r}}_\perp = \hat{\boldsymbol{\eta}} + \hat{\mathbf{R}}, \tag{S9}$$

i.e.

$$\hat{x} = \sqrt{\frac{\hbar}{2eB_0}}(\hat{a} + \hat{a}^\dagger + \hat{b} + \hat{b}^\dagger), \qquad \hat{y} = i\sqrt{\frac{\hbar}{2eB_0}}\left(\hat{a} - \hat{a}^\dagger - \hat{b} + \hat{b}^\dagger\right). \tag{S10}$$

The kinetic momentum depends only on the cyclotron sector,

$$\hat{\pi}_x = -eB_0\hat{\eta}_y = -i\sqrt{\frac{\hbar eB_0}{2}}(\hat{a} - \hat{a}^\dagger), \qquad \hat{\pi}_y = eB_0\hat{\eta}_x = \sqrt{\frac{\hbar eB_0}{2}}(\hat{a} + \hat{a}^\dagger). \tag{S11}$$

The canonical momentum $\hat{\mathbf{p}} = \hat{\boldsymbol{\pi}} - e\mathbf{A}(\hat{\mathbf{r}})$ becomes

$$\hat{p}_x = \hat{\pi}_x + \frac{eB_0}{2}\hat{y} = -\frac{i}{2}\sqrt{\frac{\hbar eB_0}{2}}\left(\hat{a} - \hat{a}^\dagger + \hat{b} - \hat{b}^\dagger\right), \quad \hat{p}_y = \hat{\pi}_y - \frac{eB_0}{2}\hat{x} = \frac{1}{2}\sqrt{\frac{\hbar eB_0}{2}}\left(\hat{a} + \hat{a}^\dagger - \hat{b} - \hat{b}^\dagger\right). \tag{S12}$$

The Landau Hamiltonian

$$\hat{H}_0 = \frac{\hat{\boldsymbol{\pi}}^2}{2m} \tag{S13}$$

reduces to

$$\hat{H}_0 = \hbar\omega_{L,0}\left(2\hat{a}^\dagger\hat{a} + 1\right), \tag{S14}$$

showing that it depends only on the cyclotron sector, while n_b labels the degeneracy.

The canonical orbital angular momentum

$$\hat{\mathcal{L}} = \hat{x}\hat{p}_y - \hat{y}\hat{p}_x \tag{S15}$$

takes the compact form

$$\hat{\mathcal{L}} = \hbar(\hat{a}^\dagger\hat{a} - \hat{b}^\dagger\hat{b}), \tag{S16}$$

so that eigenstates $|n_a, n_b\rangle$ carry quantum number $\ell = n_a - n_b$.

The extrinsic orbital angular momentum can be evaluated as follows:

$$\begin{aligned}
\mathcal{L}_{\text{ext}} &= \langle\hat{x}\rangle\langle\hat{p}_y\rangle - \langle\hat{y}\rangle\langle\hat{p}_x\rangle \\
&= \sqrt{\frac{\hbar}{2eB_0}}\left(\langle\hat{a}\rangle + \langle\hat{a}^\dagger\rangle + \langle\hat{b}\rangle + \langle\hat{b}^\dagger\rangle\right) \times \frac{1}{2}\sqrt{\frac{\hbar eB_0}{2}}\left(\langle\hat{a}\rangle + \langle\hat{a}^\dagger\rangle - \langle\hat{b}\rangle - \langle\hat{b}^\dagger\rangle\right) \\
&\quad - i\sqrt{\frac{\hbar}{2eB_0}}\left(\langle\hat{a}\rangle - \langle\hat{a}^\dagger\rangle - \langle\hat{b}\rangle + \langle\hat{b}^\dagger\rangle\right) \times \left(-\frac{i}{2}\right)\sqrt{\frac{\hbar eB_0}{2}}\left(\langle\hat{a}\rangle - \langle\hat{a}^\dagger\rangle + \langle\hat{b}\rangle - \langle\hat{b}^\dagger\rangle\right) \\
&= \hbar\left(\langle\hat{a}\rangle\langle\hat{a}^\dagger\rangle - \langle\hat{b}\rangle\langle\hat{b}^\dagger\rangle\right) \\
&= \hbar\left(|\langle\hat{a}\rangle|^2 - |\langle\hat{b}^\dagger\rangle|^2\right)
\end{aligned} \tag{S17}$$

Finally,

$$\hat{r}_\perp^2 = \hat{x}^2 + \hat{y}^2 = \frac{2\hbar}{eB_0}\left(\hat{a}^\dagger\hat{a} + \hat{b}^\dagger\hat{b} + \hat{a}\hat{b} + \hat{a}^\dagger\hat{b}^\dagger + 1\right). \tag{S18}$$

S2. EFFECTIVE HAMILTONIAN AND SU(1,1) STRUCTURE

A. Decomposition of the effective Hamiltonian

The paraxial effective Hamiltonian for an axisymmetric nonuniform magnetic field reads

$$\hat{H}_{\rm eff}(z) = \frac{\hat{\mathbf{p}}_\perp^2}{2m} + \omega_L(z)\hat{\mathcal{L}} + \frac{1}{2}m\omega_L^2(z)\,\hat{r}_\perp^2, \tag{S19}$$

with $\omega_L(z) = eB(z)/2m$ and $\hat{\mathcal{L}} = \hat{x}\hat{p}_y - \hat{y}\hat{p}_x$. We fix a reference plane z_0 and write $\omega_L(z) = \omega_L(z_0) + \Omega(z)$, with $\Omega(z) \equiv \omega_L(z) - \omega_L(z_0)$. The z_0 terms are regrouped as

$$\frac{\hat{\mathbf{p}}_\perp^2}{2m} + \omega_L(z_0)\hat{\mathcal{L}} + \frac{1}{2}m\omega_L^2(z_0)\,\hat{r}_\perp^2 = \hat{H}_0, \tag{S20}$$

where $\hat{H}_0$ is diagonal in the Fock basis $|n_a, n_b\rangle$. Substituting this decomposition into (S19) yields

$$\hat{H}_{\rm eff}(z) = \hat{H}_0 + \Omega(z)\hat{\mathcal{L}} + \frac{1}{2}m\big[\omega_L^2(z) - \omega_L^2(z_0)\big]\hat{r}_\perp^2. \tag{S21}$$

B. SU(1,1) structure

The squared transverse radius expressed in Landau ladder operators is

$$\hat{r}_\perp^2 = \frac{2\hbar}{eB_0}\big(2\hat{K}_0 + \hat{K}_- + \hat{K}_+\big), \tag{S22}$$

where $B_0 = B(z_0)$ and the SU(1,1) generators are

$$\hat{K}_0 = \tfrac{1}{2}(\hat{a}^\dagger\hat{a} + \hat{b}^\dagger\hat{b} + 1), \qquad \hat{K}_+ = \hat{a}^\dagger\hat{b}^\dagger, \qquad \hat{K}_- = \hat{a}\hat{b}, \tag{S23}$$

satisfying $[\hat{K}_0, \hat{K}_\pm] = \pm\hat{K}_\pm$ and $[\hat{K}_-, \hat{K}_+] = 2\hat{K}_0$. Using $eB_0 = 2m\omega_L(z_0)$, the perturbation becomes

$$\begin{aligned}\frac{1}{2}m\big[\omega_L^2(z) - \omega_L^2(z_0)\big]\hat{r}_\perp^2 &= \frac{1}{2}m\big[\omega_L^2(z) - \omega_L^2(z_0)\big]\frac{2\hbar}{2m\omega_L(z_0)}\big(2\hat{K}_0 + \hat{K}_- + \hat{K}_+\big)\\ &= \Lambda(z)\big(2\hat{K}_0 + \hat{K}_- + \hat{K}_+\big),\end{aligned} \tag{S24}$$

where

$$\Lambda(z) \equiv \frac{\hbar\big[\omega_L^2(z) - \omega_L^2(z_0)\big]}{2\omega_L(z_0)}. \tag{S25}$$

The canonical OAM commutes with all SU(1,1) generators:

$$[\hat{\mathcal{L}}, \hat{K}_0] = 0, \qquad [\hat{\mathcal{L}}, \hat{K}_\pm] = 0. \tag{S26}$$

The first follows from $[\hat{\mathcal{L}}, \hat{a}^\dagger\hat{a}] = [\hat{\mathcal{L}}, \hat{b}^\dagger\hat{b}] = 0$. For $\hat{K}_+ = \hat{a}^\dagger\hat{b}^\dagger$, $[\hat{\mathcal{L}}, \hat{K}_+] = [\hat{\mathcal{L}}, \hat{a}^\dagger]\hat{b}^\dagger + \hat{a}^\dagger[\hat{\mathcal{L}}, \hat{b}^\dagger] = (\hbar\hat{a}^\dagger)\hat{b}^\dagger + \hat{a}^\dagger(-\hbar\hat{b}^\dagger) = 0$, and similarly for $\hat{K}_-$. Thus the complete z-dependent part takes the form

$$\hat{V}(z) = \Omega(z)\hat{\mathcal{L}} + \Lambda(z)\big(2\hat{K}_0 + \hat{K}_- + \hat{K}_+\big). \tag{S27}$$

C. Factorization of the unitary transformation

The term $\hat{H}_0 + \Omega(z)\hat{\mathcal{L}}$ can be removed by

$$\hat{U}(z) = \exp\Big[-\frac{i}{\hbar v}\int_{z_0}^{z} dz'\,\big(\hat{H}_0 + \Omega(z')\hat{\mathcal{L}}\big)\Big]. \tag{S28}$$

Since $[\hat{H}_0, \hat{\mathcal{L}}] = 0$, the exponential factorizes:

$$\hat{U}(z) = \exp\Big(-\frac{i}{\hbar v}\hat{H}_0(z-z_0)\Big)\ \exp\Big(-\frac{i}{\hbar v}\int_{z_0}^{z} dz'\,\Omega(z')\hat{\mathcal{L}}\Big) \equiv \hat{U}_0(z)\,\hat{U}_L(z). \tag{S29}$$

The required commutators are

$$[\hat{H}_0, \hat{a}] = -2\hbar\omega_L(z_0)\hat{a}, \qquad [\hat{H}_0, \hat{b}^\dagger] = 0, \tag{S30}$$

$$[\hat{\mathcal{L}}, \hat{a}] = -\hbar\hat{a}, \qquad [\hat{\mathcal{L}}, \hat{b}^\dagger] = -\hbar\hat{b}^\dagger. \tag{S31}$$

A BCH calculation gives the combined transformation

$$\hat{U}^\dagger(z)\,\hat{a}\,\hat{U}(z) = \hat{a}\,e^{-i[\Phi(z)+\Phi_1(z)]}, \tag{S32}$$

$$\hat{U}^\dagger(z)\,\hat{b}^\dagger\,\hat{U}(z) = \hat{b}^\dagger\,e^{-i\Phi_1(z)}, \tag{S33}$$

where

$$\Phi(z) = \frac{2\omega_L(z_0)(z-z_0)}{v}, \qquad \Phi_1(z) = \frac{1}{v}\int_{z_0}^{z} dz'\,\Omega(z'). \tag{S34}$$

D. Transformation of the SU(1,1) generators

Since $[\hat{\mathcal{L}}, \hat{K}_\pm] = 0$, the Φ_1 phases cancel in $\hat{K}_\pm$:

$$\hat{U}^\dagger\hat{K}_0\hat{U} = \hat{K}_0, \tag{S35}$$

$$\hat{U}^\dagger\hat{K}_\pm\hat{U} = \hat{K}_\pm\,e^{\pm i\Phi(z)}. \tag{S36}$$

E. Interaction picture

The Schrödinger-picture state satisfies $i\hbar v\,\partial_z|\chi(z)\rangle = \hat{H}_{\rm eff}(z)|\chi(z)\rangle$. Defining $|\chi_I(z)\rangle = \hat{U}^\dagger(z)|\chi(z)\rangle$, a standard calculation gives

$$i\hbar v\,\partial_z|\chi_I(z)\rangle = \hat{H}_I(z)|\chi_I(z)\rangle, \tag{S37}$$

with

$$\hat{H}_I(z) = \Lambda(z)\big(2\hat{K}_0 + e^{-i\Phi}\hat{K}_- + e^{i\Phi}\hat{K}_+\big). \tag{S38}$$

F. Heisenberg equations in the interaction frame

Introducing $\hat{U}_I(z)$ via $i\hbar v\,\partial_z\hat{U}_I = \hat{H}_I\hat{U}_I$, $\hat{U}_I(z_0) = I$, the Heisenberg operators are

$$\hat{a}_I(z) = \hat{U}_I^\dagger(z)\hat{a}\,\hat{U}_I(z), \qquad \hat{b}_I^\dagger(z) = \hat{U}_I^\dagger(z)\hat{b}^\dagger\,\hat{U}_I(z). \tag{S39}$$

Using $[\hat{a}, \hat{K}_0] = \frac{1}{2}\hat{a}$, $[\hat{a}, \hat{K}_-] = 0$, $[\hat{a}, \hat{K}_+] = \hat{b}^\dagger$, one finds

$$i\hbar v\,\partial_z\hat{a}_I = \Lambda\big(\hat{a}_I + e^{i\Phi}\hat{b}_I^\dagger\big), \tag{S40}$$

$$i\hbar v\,\partial_z\hat{b}_I^\dagger = -\Lambda\big(\hat{b}_I^\dagger + e^{-i\Phi}\hat{a}_I\big). \tag{S41}$$

G. Rotating frame and conserved norm

The symmetric rotation $\hat{a}_R = e^{-i\Phi/2}\hat{a}_I$, $\hat{b}_R^\dagger = e^{i\Phi/2}\hat{b}_I^\dagger$ removes the oscillating phases, yielding $i\hbar v\,\partial_z(\hat{a}_R, \hat{b}_R^\dagger)^T = \mathcal{H}(z)(\hat{a}_R, \hat{b}_R^\dagger)^T$ with

$$\mathcal{H}(z) = \begin{pmatrix} \Delta(z) & \Lambda(z) \\ -\Lambda(z) & -\Delta(z) \end{pmatrix}, \quad \Delta(z) = \hbar\omega_L(z_0) + \Lambda(z). \tag{S42}$$

Since $\mathcal{H}^\dagger\sigma_z = \sigma_z\mathcal{H}$, the SU(1,1) norm

$$|\langle\hat{a}_R\rangle_0|^2 - |\langle\hat{b}_R^\dagger\rangle_0|^2 = \text{const}, \tag{S43}$$

where $\langle\cdot\rangle_0 \equiv \langle\chi_I(z_0)|\cdot|\chi_I(z_0)\rangle$.

H. Return to the Schrödinger picture

We now trace the sequence of unitary transformations backwards to relate the conserved SU(1,1) norm to the Schrödinger-picture expectation values, which are directly connected to the extrinsic OAM via $\mathcal{L}_{\text{ext}}/\hbar = |\langle\hat{a}\rangle|^2 - |\langle\hat{b}^\dagger\rangle|^2$.

Recall the three layers of the construction:

- Schrödinger picture: state $|\chi(z)\rangle$, fixed operators $\hat{a}, \hat{b}^\dagger$.
- Interaction picture: $|\chi_I(z)\rangle = \hat{U}^\dagger(z)|\chi(z)\rangle$, fixed operators $\hat{a}, \hat{b}^\dagger$.
- Heisenberg-in-interaction picture: fixed state $|\chi_I(z_0)\rangle$, evolving operators $\hat{a}_I(z) = \hat{U}_I^\dagger(z)\,\hat{a}\,\hat{U}_I(z)$, $\hat{b}_I^\dagger(z) = \hat{U}_I^\dagger(z)\,\hat{b}^\dagger\,\hat{U}_I(z)$.

The rotating-frame operators are $\hat{a}_R = e^{-i\Phi/2}\hat{a}_I$, $\hat{b}_R^\dagger = e^{i\Phi/2}\hat{b}_I^\dagger$, and $\langle\cdot\rangle_0 \equiv \langle\chi_I(z_0)|\cdot|\chi_I(z_0)\rangle$.

Because $[\hat{H}_0 + \Omega\hat{\mathcal{L}}, \hat{a}] \propto \hat{a}$ and $[\hat{H}_0 + \Omega\hat{\mathcal{L}}, \hat{b}^\dagger] \propto \hat{b}^\dagger$, both $\hat{a}$ and $\hat{b}^\dagger$ are eigenoperators of the unitary $\hat{U}(z)$. Consequently, $\hat{U}$ and $\hat{U}^\dagger$ act on them by simple phase factors: $\hat{U}^\dagger\hat{a}\,\hat{U} = \hat{a}\,e^{-i[\Phi+\Phi_1]}$ and $\hat{U}\hat{a}\,\hat{U}^\dagger = \hat{a}\,e^{+i[\Phi+\Phi_1]}$, and similarly for $\hat{b}^\dagger$ with phase Φ_1.

Unwinding the transformations for $\langle\hat{a}_R\rangle_0$ step by step:

$$\begin{aligned}
\langle\hat{a}_R(z)\rangle_0 &= e^{-i\Phi/2}\,\langle\chi_I(z_0)|\,\hat{U}_I^\dagger(z)\,\hat{a}\,\hat{U}_I(z)\,|\chi_I(z_0)\rangle \\
&= e^{-i\Phi/2}\,\langle\chi_I(z)|\,\hat{a}\,|\chi_I(z)\rangle \qquad \big(|\chi_I(z)\rangle = \hat{U}_I(z)|\chi_I(z_0)\rangle\big) \\
&= e^{-i\Phi/2}\,\langle\chi(z)|\,\hat{U}(z)\,\hat{a}\,\hat{U}^\dagger(z)\,|\chi(z)\rangle \qquad \big(|\chi_I(z)\rangle = \hat{U}^\dagger(z)|\chi(z)\rangle\big) \\
&= e^{-i\Phi/2}\,e^{+i[\Phi+\Phi_1]}\,\langle\chi(z)|\hat{a}|\chi(z)\rangle \\
&= e^{+i[\Phi/2+\Phi_1]}\,\langle\hat{a}\rangle.
\end{aligned} \tag{S44}$$

For $\langle\hat{b}_R^\dagger\rangle_0$ the same steps give

$$\begin{aligned}
\langle\hat{b}_R^\dagger(z)\rangle_0 &= e^{+i\Phi/2}\,\langle\chi_I(z_0)|\,\hat{U}_I^\dagger(z)\,\hat{b}^\dagger\,\hat{U}_I(z)\,|\chi_I(z_0)\rangle \\
&= e^{+i\Phi/2}\,\langle\chi_I(z)|\,\hat{b}^\dagger\,|\chi_I(z)\rangle \\
&= e^{+i\Phi/2}\,\langle\chi(z)|\,\hat{U}(z)\,\hat{b}^\dagger\,\hat{U}^\dagger(z)\,|\chi(z)\rangle \\
&= e^{+i\Phi/2}\,e^{+i\Phi_1}\,\langle\chi(z)|\hat{b}^\dagger|\chi(z)\rangle \\
&= e^{+i[\Phi/2+\Phi_1]}\,\langle\hat{b}^\dagger\rangle.
\end{aligned} \tag{S45}$$

Both expectation values carry the *same* overall phase factor $e^{+i[\Phi/2+\Phi_1]}$.

S3. TIME EVOLUTION OF THE EXTRINSIC OAM

A. Heisenberg equations

The full Hamiltonian in the symmetric gauge is

$$\hat{H} = \frac{\hat{\mathbf{p}}^2}{2m} + \hat{\omega}_L\,\hat{\mathcal{L}} + \frac{1}{2}m\,\hat{\omega}_L^2\,\hat{r}_\perp^2, \qquad \hat{\omega}_L \equiv \omega_L(\hat{z}) = \frac{e}{2m}B(\hat{z}), \tag{S46}$$

with $\hat{\mathcal{L}} = \hat{x}\hat{p}_y - \hat{y}\hat{p}_x$ and $\hat{r}_\perp^2 = \hat{x}^2 + \hat{y}^2$.

From $\frac{d}{dt}\langle\hat{O}\rangle = \frac{i}{\hbar}\langle[\hat{H},\hat{O}]\rangle$, using $[\hat{\mathcal{L}},\hat{x}] = i\hbar\hat{y}$, $[\hat{\mathcal{L}},\hat{y}] = -i\hbar\hat{x}$, $[\hat{\mathcal{L}},\hat{p}_x] = i\hbar\hat{p}_y$, and $[\hat{\mathcal{L}},\hat{p}_y] = -i\hbar\hat{p}_x$:

$$[\hat{H},\hat{x}] = \frac{1}{2m}[\hat{p}_x^2,\hat{x}] + \hat{\omega}_L[\hat{\mathcal{L}},\hat{x}] = -\frac{i\hbar}{m}\hat{p}_x + i\hbar\hat{\omega}_L\hat{y} = -\frac{i\hbar}{m}\hat{\pi}_x \quad\Rightarrow\quad \frac{d\langle\hat{x}\rangle}{dt} = \frac{\langle\hat{\pi}_x\rangle}{m}, \tag{S47}$$

$$[\hat{H},\hat{y}] = -\frac{i\hbar}{m}\hat{p}_y - i\hbar\hat{\omega}_L\hat{x} = -\frac{i\hbar}{m}\hat{\pi}_y \quad\Rightarrow\quad \frac{d\langle\hat{y}\rangle}{dt} = \frac{\langle\hat{\pi}_y\rangle}{m}, \tag{S48}$$

$$[\hat{H},\hat{p}_x] = \hat{\omega}_L[\hat{\mathcal{L}},\hat{p}_x] + \frac{1}{2}m\hat{\omega}_L^2[\hat{x}^2,\hat{p}_x] = i\hbar\big(\hat{\omega}_L\hat{p}_y + m\hat{\omega}_L^2\hat{x}\big) \quad\Rightarrow\quad \frac{d\langle\hat{p}_x\rangle}{dt} = -\langle\hat{\omega}_L\hat{p}_y\rangle - m\langle\hat{\omega}_L^2\hat{x}\rangle, \tag{S49}$$

$$[\hat{H},\hat{p}_y] = -i\hbar\big(\hat{\omega}_L\hat{p}_x - m\hat{\omega}_L^2\hat{y}\big) \quad\Rightarrow\quad \frac{d\langle\hat{p}_y\rangle}{dt} = \langle\hat{\omega}_L\hat{p}_x\rangle - m\langle\hat{\omega}_L^2\hat{y}\rangle, \tag{S50}$$

with the kinetic (mechanical) momenta

$$\hat{\pi}_x = \hat{p}_x - m\hat{\omega}_L\hat{y}, \qquad \hat{\pi}_y = \hat{p}_y + m\hat{\omega}_L\hat{x}. \tag{S51}$$

These equations are exact consequences of $\hat{H}$; no approximation to the quantum dynamics has been made.

B. Evolution of the extrinsic OAM

Differentiating $\mathcal{L}_{\rm ext} = \langle\hat{x}\rangle\langle\hat{p}_y\rangle - \langle\hat{y}\rangle\langle\hat{p}_x\rangle$ and inserting the Heisenberg equations,

$$\begin{aligned}\frac{d\mathcal{L}_{\rm ext}}{dt} &= \frac{\langle\hat{\pi}_x\rangle}{m}\langle\hat{p}_y\rangle + \langle\hat{x}\rangle\big(\langle\hat{\omega}_L\hat{p}_x\rangle - m\langle\hat{\omega}_L^2\hat{y}\rangle\big) - \frac{\langle\hat{\pi}_y\rangle}{m}\langle\hat{p}_x\rangle - \langle\hat{y}\rangle\big(-\langle\hat{\omega}_L\hat{p}_y\rangle - m\langle\hat{\omega}_L^2\hat{x}\rangle\big)\\ &= \frac{1}{m}\big[\langle\hat{\pi}_x\rangle\langle\hat{p}_y\rangle - \langle\hat{\pi}_y\rangle\langle\hat{p}_x\rangle\big] + \big[\langle\hat{x}\rangle\langle\hat{\omega}_L\hat{p}_x\rangle + \langle\hat{y}\rangle\langle\hat{\omega}_L\hat{p}_y\rangle\big]\\ &\quad + m\big[\langle\hat{y}\rangle\langle\hat{\omega}_L^2\hat{x}\rangle - \langle\hat{x}\rangle\langle\hat{\omega}_L^2\hat{y}\rangle\big].\end{aligned} \tag{S52}$$

The kinematic bracket is then expanded via (S51). The purely canonical parts cancel trivially, while the gauge-potential contributions give

$$\frac{1}{m}\big[\langle\hat{\pi}_x\rangle\langle\hat{p}_y\rangle - \langle\hat{\pi}_y\rangle\langle\hat{p}_x\rangle\big] = -\big[\langle\hat{\omega}_L\hat{x}\rangle\langle\hat{p}_x\rangle + \langle\hat{\omega}_L\hat{y}\rangle\langle\hat{p}_y\rangle\big]. \tag{S53}$$

Inserting this result back and grouping terms with the same operator content yields the exact intermediate form

$$\begin{aligned}\frac{d\mathcal{L}_{\rm ext}}{dt} &= m\big[\langle\hat{y}\rangle\langle\hat{\omega}_L^2\hat{x}\rangle - \langle\hat{x}\rangle\langle\hat{\omega}_L^2\hat{y}\rangle\big]\\ &\quad + \big[\langle\hat{x}\rangle\langle\hat{\omega}_L\hat{p}_x\rangle - \langle\hat{\omega}_L\hat{x}\rangle\langle\hat{p}_x\rangle\big]\\ &\quad + \big[\langle\hat{y}\rangle\langle\hat{\omega}_L\hat{p}_y\rangle - \langle\hat{\omega}_L\hat{y}\rangle\langle\hat{p}_y\rangle\big].\end{aligned} \tag{S54}$$

To expose the role of correlations we introduce the covariance $\mathrm{Cov}(\hat{o}_1,\hat{o}_2) = \langle\hat{o}_1\hat{o}_2\rangle - \langle\hat{o}_1\rangle\langle\hat{o}_2\rangle$. Writing each average as a covariance plus a factorized contribution,

$$\begin{aligned}\langle\hat{x}\rangle\langle\hat{\omega}_L\hat{p}_x\rangle - \langle\hat{\omega}_L\hat{x}\rangle\langle\hat{p}_x\rangle &= \langle\hat{x}\rangle\big[\mathrm{Cov}(\hat{\omega}_L,\hat{p}_x) + \langle\hat{\omega}_L\rangle\langle\hat{p}_x\rangle\big] - \big[\mathrm{Cov}(\hat{\omega}_L,\hat{x}) + \langle\hat{\omega}_L\rangle\langle\hat{x}\rangle\big]\langle\hat{p}_x\rangle\\ &= \langle\hat{x}\rangle\,\mathrm{Cov}(\hat{\omega}_L,\hat{p}_x) - \langle\hat{p}_x\rangle\,\mathrm{Cov}(\hat{\omega}_L,\hat{x}),\end{aligned} \tag{S55}$$

the pieces $\langle\hat{x}\rangle\langle\hat{\omega}_L\rangle\langle\hat{p}_x\rangle$ cancelling pairwise. The remaining two brackets are transformed in the same way. For the $m[\cdots]$ part one expands

$$m\langle\hat{y}\rangle\langle\hat{\omega}_L^2\hat{x}\rangle = m\langle\hat{y}\rangle\big[\mathrm{Cov}(\hat{\omega}_L^2,\hat{x}) + \langle\hat{\omega}_L^2\rangle\langle\hat{x}\rangle\big], \tag{S56}$$

$$m\langle\hat{x}\rangle\langle\hat{\omega}_L^2\hat{y}\rangle = m\langle\hat{x}\rangle\big[\mathrm{Cov}(\hat{\omega}_L^2,\hat{y}) + \langle\hat{\omega}_L^2\rangle\langle\hat{y}\rangle\big], \tag{S57}$$

and the terms containing $\langle\hat{\omega}_L^2\rangle$ cancel identically because $\langle\hat{y}\rangle\langle\hat{x}\rangle - \langle\hat{x}\rangle\langle\hat{y}\rangle = 0$. Collecting everything,

$$\begin{aligned}\frac{d\mathcal{L}_{\mathrm{ext}}}{dt} &= m\big[\langle\hat{y}\rangle\,\mathrm{Cov}(\hat{\omega}_L^2,\hat{x}) - \langle\hat{x}\rangle\,\mathrm{Cov}(\hat{\omega}_L^2,\hat{y})\big] \\ &\quad + \big[\langle\hat{x}\rangle\,\mathrm{Cov}(\hat{\omega}_L,\hat{p}_x) - \langle\hat{p}_x\rangle\,\mathrm{Cov}(\hat{\omega}_L,\hat{x})\big] \\ &\quad + \big[\langle\hat{y}\rangle\,\mathrm{Cov}(\hat{\omega}_L,\hat{p}_y) - \langle\hat{p}_y\rangle\,\mathrm{Cov}(\hat{\omega}_L,\hat{y})\big].\end{aligned} \tag{S58}$$

S4. FIRST-PRINCIPLES NUMERICAL SIMULATIONS

A. Propagation algorithm and initial-state wavefunction

We develop a numerical solver for the three-dimensional time-dependent magnetic Schrödinger equation for a scalar electron

$$i\hbar\partial_t\psi = \hat{H}\psi, \quad \hat{H} = \frac{\hat{\boldsymbol{\pi}}^2}{2m} = -\frac{\hbar^2}{2m}\nabla^2 - i\hbar\frac{e}{m}(\mathbf{A}\cdot\boldsymbol{\nabla}) + \frac{e^2}{2m}\mathbf{A}^2, \tag{S59}$$

provided the Coulomb gauge condition $\nabla\cdot\mathbf{A} = 0$ is satisfied. Then we perform first-principles simulations of single-electron wavefunctions in coherent vortex states.

In our code, we employ the Strang-splitting scheme temporal discretization, which is third-order accurate and symplectic, and the Fourier pseudo-spectral method for spatial discretization, which is spectrally accurate, based upon the FFT (Fast Fourier Transform) techniques. For correctly treating the paramagnetic operator $(\mathbf{A}\cdot\nabla)$, the so-called semi-Lagrangian method is adopted in combination with 5th-order spline interpolation, which is an unconditionally stable technique commonly used in dealing with advection problems. This design strikes an optimal balance between computational efficiency and solution accuracy, making it a robust tool for solving various Schrödinger-type wave equations. Additionally, all the expectation values are computed via trapezoidal quadrature that gives second-order accurate results.

The numerical scheme for each time-step that we constructed, in theory, is formulated as

$$\psi_1(\mathbf{r}) = \mathcal{F}^{-1}\left[\exp\left[\frac{\hbar\Delta t}{4im}\mathbf{k}^2\right]\mathcal{F}[\psi(t,\mathbf{r})]\right] \tag{S60a}$$

$$\psi_2(\mathbf{r}) = \exp\left[\frac{e^2\Delta t}{4im\hbar}\mathbf{A}^2(\mathbf{r})\right]\psi_1(\mathbf{r}) \tag{S60b}$$

$$\psi_3(\mathbf{r}) = \psi_2(\mathbf{s}(t)) \ \text{ for } \left\{\begin{array}{l}\dfrac{\mathrm{d}\mathbf{s}(t)}{\mathrm{d}t} = \dfrac{-e}{m}\mathbf{A}(t,\mathbf{s}(t)),\\ \mathbf{s}(t+\Delta t) = \mathbf{r}\end{array}\right\} \tag{S60c}$$

$$\psi_4(\mathbf{r}) = \exp\left[\frac{e^2\Delta t}{4im\hbar}\mathbf{A}^2(\mathbf{r})\right]\psi_3(\mathbf{r}) \tag{S60d}$$

$$\psi(t+\Delta t,\mathbf{r}) \approx \mathcal{F}^{-1}\left[\exp\left[\frac{\hbar\Delta t}{4im}\mathbf{k}^2\right]\mathcal{F}[\psi_4(\mathbf{r})]\right]. \tag{S60e}$$

Here $\mathbf{r} = (x,y,z)^T$ and $\mathbf{k} = (k_x,k_y,k_z)^T$ mean rectangular grid-points in discrete 3-dimensional real space and the related wavenumber space in the code. The operators $\mathcal{F}$ and $\mathcal{F}^{-1}$ denote the Fourier transformation from $\mathbf{r}$-space to $\mathbf{k}$-space and its inversion—FFT algorithms in practice. The third line represents a solution to the advection sub-problem $\partial_t\psi + \frac{e}{m}(\mathbf{A}\cdot\nabla)\psi = 0$ by semi-Lagrangian method. Essentially, this scheme primarily involves a traceback procedure (solving the set of ODEs) followed by a coordinate mapping (to update the wavefunction) for each time-step. In our code, the traceback procedure computes the corresponding interpolation coordinate $\mathbf{s}$ for each spatial grid-point $\mathbf{r}$. Then, the coordinate mapping $\psi(t+\Delta t,\mathbf{r}) = \psi(t,\mathbf{s})$ implies that value of $\psi(t+\Delta t)$ at grid-point $\mathbf{r}$ equals the estimated value of $\psi(t)$ at the associated interpolation point $\mathbf{s}$.

At $t = 0$, the electron wavefunction is initiated with a Laguerre-Gaussian wavefront and a helical phase plus a Gaussian longitudinal envelope, centered at $\mathbf{r}_0$, with mean velocity v_0. The initial wavefunction is formulated as

$$\begin{aligned}
&\mathbf{r}' = \mathbf{r} - \mathbf{r}_0,\ r'_\perp = \sqrt{x'^2+y'^2},\ \theta' = \arctan[y'/x'],\\
&\psi_0 = \mathcal{N}_\perp\frac{(r'_\perp)^{|\ell|}}{w_\perp^{|\ell|+1}}L_n^{|\ell|}\left[\frac{(r'_\perp)^2}{w_\perp^2}\right]\exp\left[-\frac{(r'_\perp)^2}{2w_\perp^2} + \mathrm{i}\ell\theta'\right]\\
&\qquad\times\frac{\mathcal{N}_z}{\sqrt{w_z}}\exp\left[-\frac{(z')^2}{2w_z^2} - \frac{m}{\mathrm{i}\hbar}v_0z'\right]\exp\left[\frac{e}{\mathrm{i}\hbar}\Lambda(\mathbf{r})\right],\\
&\Lambda(\mathbf{r}) = \int_{\mathbf{r}_0}^{\mathbf{r}}\mathrm{d}\mathbf{s}\cdot\mathbf{A}(\mathbf{s}) = \tfrac{1}{2}B(z)[x_0y - xy_0].
\end{aligned} \tag{S61}$$

Here $e\Lambda(\mathbf{r})/\hbar$ is a local gauge phase. $w_\perp$ and w_z are respectively the radial and axial characteristic widths of the wavepacket. $L_n^{|\ell|}[X]$ means the generalized Laguerre-Gaussian polynomial associated to radial index n and topological charge ℓ. $\mathcal{N}_\perp$ and $\mathcal{N}_z$ represent the transverse and longitudinal normalization factors, respectively.

B. Supplemental simulation results

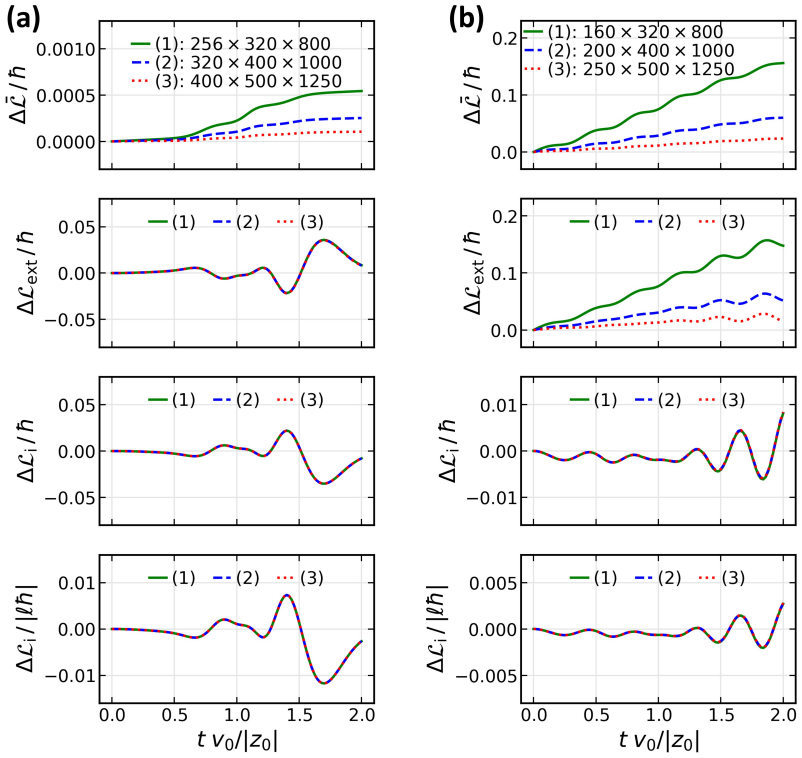


FIG. S1. Mesh-refinement tests for settings (a) associated to the case $a = 40\,w_m$ in Fig. 2 and (b) the case $y_0 = +6\,w_m$ in Fig. 3. For each column, the figure legend marks the spatial resolution $N_x \times N_y \times N_z$ of different cases with identical simulation domain. Note that we adopt a $320 \times 400 \times 1000$-resolution mesh for the simulations depicted in Fig. 2 and $200 \times 400 \times 1000$-resolution for those associated to Fig. 3 of the main context. For cases in the left column (a), a vortex wavepacket with topological charge $\ell = +3$, longitudinal speed $v_0 = 160w_m/(6T_c)$, characteristic width $w_\perp = 2\,w_m$ and length $w_z = 4\,w_m$, initially centering at $(0, +2w_m, -80w_m)$, is released in a Glaser field characterized by $a = 40\,w_m$. For cases in the right column (b), a vortex wavepacket with topological charge $\ell = +3$, characteristic width $w_\perp = 1\,w_m$ and length $w_z = 4\,w_m$, initially centering at $(0, +6w_m, -80w_m)$, is released in a Glaser field characterized by $a = 160\,w_m$ with longitudinal speed $v_0 = 160w_m/(6T_c)$ the topological charge is $\ell = +3$ and the centroid speed is $v_0 = 160w_m/(6T_c)$. All these cases apply the peak field strength $B_0 = 0.02\,\mathrm{T}$ which corresponds to characteristic beam-width $w_m = \sqrt{2\hbar/(eB_0)} = 0.256\,\mu\mathrm{m}$ and cyclotron period $T_c = 2\pi\, m/(eB_0) = 1.786\,\mathrm{ns}$. Each case experiences 100 time-steps.

Figure S1 shows the results of grid-refinement tests for the settings corresponding to the case $a = 40\,w_m$ in Fig. 2(b) and the case $y_0 = +6\,w_m$ in Fig. 3(b) of the main context, which exhibit the largest deviations in $\mathcal{L}_{\rm i}$ respectively. In our simulations, the rectangular simulation domain is discretized on a regular $N_x \times N_y \times N_z$-resolution grid mesh. In the main context, we adopt a $320 \times 400 \times 1000$-resolution mesh for the simulations shown in Fig. 2 [and also Movies S1–S3] and $200 \times 400 \times 1000$-resolution for those presented to Fig. 3 [and also Movies S4–S6]. Taking these meshes as the baseline resolutions, denser ($\times 1.25$) and coarser ($\times 0.8$) meshes lead to no appreciable change in $\Delta\mathcal{L}_{\rm i}$, thereby confirming numerical convergence of the computed intrinsic canonical OAM $\mathcal{L}_{\rm i}$ shown in Fig. 2(b) and Fig. 3(b) of the main context. These results indicate that the observed percent-level fluctuations $\Delta\mathcal{L}_{\rm i}$ are predominantly physical rather than numerical in origin.

Furthermore, since the axial component of canonical OAM is strictly conserved, the variation of its expectation value relative to the initial value i.e. $\Delta\bar{\mathcal{L}} = \langle\psi(t)|\hat{\mathcal{L}}|\psi(t)\rangle - \langle\psi(0)|\hat{\mathcal{L}}|\psi(0)\rangle$ is purely numerical error. In Fig. S1, the first row shows that $|\Delta\bar{\mathcal{L}}|$ systematically decreases with mesh refinement, demonstrating convergence of the numerical scheme.

Figure S2 presents numerical results of $\Delta\bar{\mathcal{L}}$ and $\Delta\mathcal{L}_{\rm i}$ against different characteristic magnetic variation length a of Glaser fields, initial transverse offset y_0 of the electron wavepacket centroid, and initial topological charge ℓ of the vortex state, separately. In rows (b*–c*) of Fig. S2, maximum values of $\Delta\mathcal{L}_{\rm e}$ and $\Delta\bar{\mathcal{L}}$ are roughly on the same order of magnitude. However, in these simulations, the change of $\mathcal{L}_{\rm i}$ relative to $\ell\hbar$, generally with relative variation $\lesssim 1\%$ [Figs. S2(a)], can be smaller than the instantaneous magnitude of $\Delta\bar{\mathcal{L}}$, manifesting excellent robustness of intrinsic

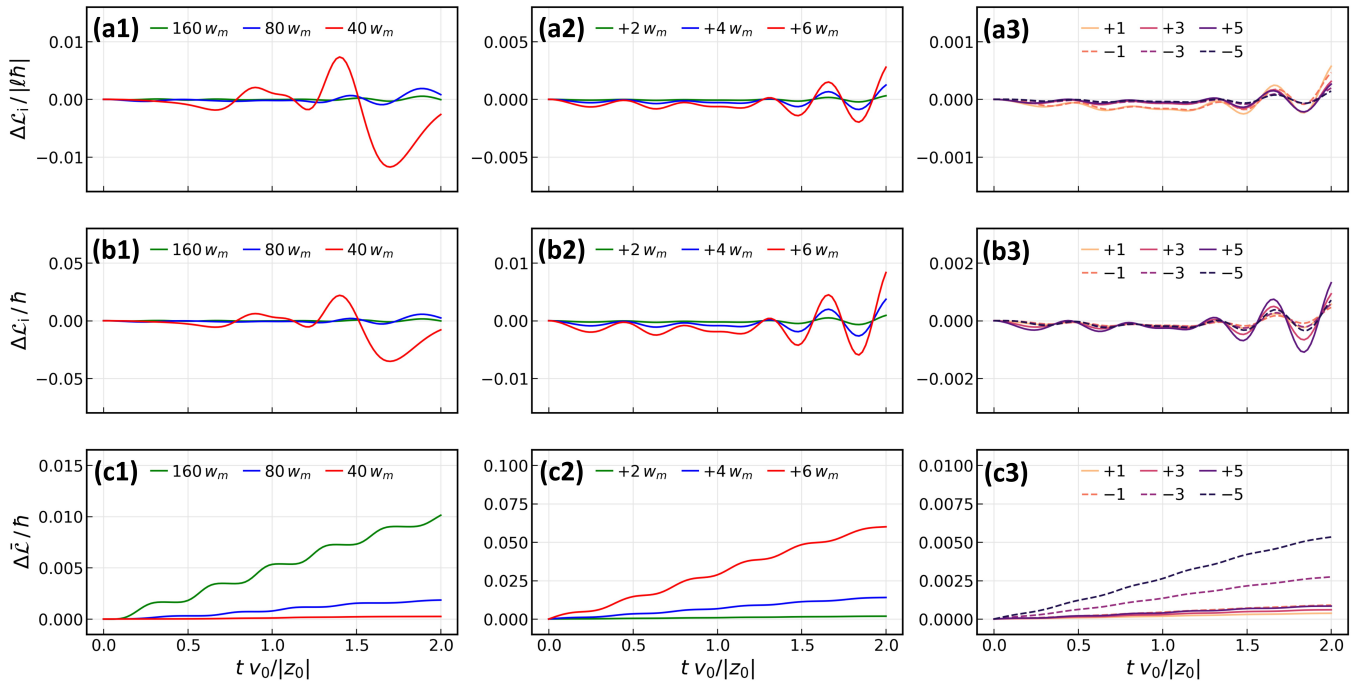


FIG. S2. (a*) Relative variation of intrinsic canonical OAM, (b*) absolute variation of intrinsic canonical OAM, and (c*) absolute variation of canonical OAM for distinct (*1) a, (*2) y_0, and (*3) ℓ. For the cases in column (*1), the initial centroid is fixed at $(0, +2, -80)\,w_m$ within Glaser fields of distinct magnetic variation distance $a \in [40, 160]\,w_m$, transverse and longitudinal spreads of the initial wavepacket are set to be $w_\perp = 2\,w_m$ and $w_z = 4\,w_m$ respectively, the topological charge is $\ell = +3$ and the centroid speed is $v_0 = 160 w_m/(6T_c)$. In column (*2), in the same Glaser field characterized by $a = 160\,w_m$, the centroid is displaced at different transverse offset $y_0 \in [+2, +6]\,w_m$ while the longitudinal coordinate of the initial centroid is $z_0 = -80\,w_m$, transverse and longitudinal spreads are $w_\perp = 1\,w_m$ and $w_z = 4\,w_m$ respectively, the topological charge is $\ell = +3$ and the centroid speed is $v_0 = 160 w_m/(6T_c)$. In column (*3), the settings, except $\ell \in [-5, +5]$, are the same as those of case $y_0 = +2\,w_m$ in (*2). In these cases, we use $B_0 = 0.02\,\mathrm{T}$ which corresponds to characteristic beam-width $w_m = \sqrt{2\hbar/(eB_0)} = 0.256\,\mu\mathrm{m}$ and cyclotron period $T_c = 2\pi\, m/(eB_0) = 1.786\,\mathrm{ns}$. The simulations shown in column (*1) are conducted within $200 \times 400 \times 1000$-resolution mesh on $20 \times 40 \times 200\,w_m^3$ rectangular space domain, and in columns (*2–3) $200 \times 200 \times 1000$-resolved $20 \times 20 \times 200\,w_m^3$ space is used. Each case experiences 100 time-steps.

canonical OAM.

The main observations may be summarized as follows:

(i) Reducing the characteristic variation length a increases the amplitude of the intrinsic-OAM oscillations. Nevertheless, the maximum relative deviation remains at the percent level for all parameters considered.

(ii) The variation amplitude grows with the transverse offset of the wavepacket centroid, yet remains below 0.3% for displacements of several characteristic beam widths.

(iii) For $\ell \in [-5, +5]$, the maximum relative deviation stays below 0.1%, and no systematic scaling with the topological charge is observed.

S5. DESCRIPTION OF SUPPLEMENTAL VIDEOS

The movies below show the time evolution of the real-space wavefunction of a vortex electron. The orthogonal planes intersect at the instantaneous wavepacket centroid, $\bar{\mathbf{r}} = \langle\psi|\hat{\mathbf{r}}|\psi\rangle$. The hue represents the phase of the complex wavefunction, $\theta = \arg[\psi]$, while the lightness is proportional to the normalized probability density, $\rho = |\psi|^2$.

Movie S1: Wavefunction of vortex electron depicted in Fig. 2(d).

Movie S2: Wavefunction of vortex electron depicted in Fig. 2(e).

Movie S3: Wavefunction of vortex electron depicted in Fig. 2(f).

Movie S4: Wavefunction of vortex electron depicted in Fig. 3(d).

Movie S5: Wavefunction of vortex electron depicted in Fig. 3(e).

Movie S6: Wavefunction of vortex electron depicted in Fig. 3(f).